Local structure and influence of bonding on the phase-change behavior of the chalcogenide compounds $K_{1-x}Rb_xSb_5S_8$

J.B. Wachter[a], K. Chrissafis[b], V. Petkov[d], C.D. Malliakas[a], D. Bilc[d], Th. Kyratsi[a,1],
K.M. Paraskevopoulos[b], S.D. Mahanti[c], T. Torbrügge[e], H. Eckert[e], M.G. Kanatzidis[a,*]

[a]Department of Chemistry, Michigan State University, East Lansing, MI 48824, USA
[b]Department of Physics, Aristotle University of Thessaloniki, 54124 Thessaloniki, Greece
[c]Department of Physics, Michigan State University, East Lansing, MI 48824, USA
[d]Department of Physics, Central Michigan University, Mount Pleasant, MI 48859, USA
[e]Institut für Physikalische Chemie, Westf. Wilhelms-Universität Münster, Germany

Abstract

KSb_5S_8 and its solid solution analogs with Rb and Tl were found to exhibit a reversible and tunable glass→crystal→glass phase transition. Selected members of this series were analyzed by differential scanning calorimetry to measure the effect of the substitution on the thermal properties. The solid solutions $K_{1-x}Rb_xSb_5S_8$ exhibited clear deviations in melting and crystallization behavior and temperatures from the parent structure. The crystallization process of the glassy KSb_5S_8 as a function of temperature could clearly be followed with Raman spectroscopy. The thermal conductivity of both glassy and crystalline KSb_5S_8 at room temperature is ∼0.40 W/m K, among the lowest known values for any dense solid-state material. Electronic band structure calculations carried out on KSb_5S_8 and $TlSb_5S_8$ show the presence of large indirect band-gaps and confirm the coexistence of covalent Sb-S bonding and predominantly ionic K(Tl)···S bonding. Pair distribution function analyses based on total X-ray scattering data on both crystalline and glassy $K_{1-x}Rb_xSb_5S_8$ showed that the basic structure-defining unit is the same and it involves a distorted polyhedron of "SbS_7" fragment of ∼7 Å diameter. The similarity of local structure between the glassy and crystalline phases accounts for the facile crystallization rate in this system.
© 2006 Elsevier Inc. All rights reserved.

Keywords: Glasses; Non-volatile memory

1. Introduction

Phase-change materials are gaining increasing interest because of their use in the data storage media crucial to the information technology industry [1,2]. These materials exhibit reversible glass-to-crystal phase transitions and can be used in applications as diverse as non-volatile memory [3], digital video disks [4], polarized holograms [5], opto-mechanical actuators [6] and infrared optical wave-guides [7]. There are two major classes of phase-change

materials: stoichiometric and non-stoichiometric. Stoichiometric phase-change materials, such as the industry standard $Ge_2Sb_2Te_5$ [8], consist of a single crystallographically distinct structure, which is recovered in pure form upon recrystallization. Non-stoichiometric glasses tend to crystallize into a mixture of two or more structures. An example of this is the $(Li_2S)_x(Sb_2S_3)_{1-x}$, $x = 0$–0.17 system, which crystallizes into a mixture of α-$LiSbS_2$ and Sb_2S_3 [9]. Stoichiometric materials are preferable due to faster crystallization rates, better cyclability and long lifetimes.

The compound KSb_5S_8 is isostructural to $TlSb_5S_8$, the mineral parapierrotite, and is a phase-change material with a rapid and reversible glass-to-crystal transition [10]. The crystalline phase melts at 441 °C and can be quenched to a glass. Upon subsequent heating, there is a glass transition

---

*Corresponding author. Fax: +1 847 491 5937.
E-mail address: m-kanatzidis@northwestern.edu (M.G. Kanatzidis).
[1]Present address: Department of Mechanical and Manufacturing Engineering, University of Cyprus, Nicosia, Cyprus.

at 223 °C followed by a rapid crystallization at 287 °C. Its structure is made of undulating $[Sb_5S_8]^-$ layers with K^+ ions seated in between the layers. The layers, however, interact strongly with one another forming essentially a three-dimensional $[Sb_5S_8]^-$ network, Fig. 1(a) [11]. This system is an interesting study case because it presents an intimate combination of covalent bonding (i.e. Sb–S bonds) and ionic K–S bonding, both of which can influence the phase-change behavior. Understanding glass crystallization in pure phases and the relationship of structure and bonding to the rates of phase change will lead to a better design of phase-change materials for specific applications. Almost all materials that have been studied so far possess exclusively covalent bond frameworks. KSb_5S_8 is a semiconductor with a band gap of 1.82 eV for the crystalline phase and 1.67 eV for the glass. The activation energy

of crystallization for KSb_5S_8 is $\sim167\pm3$ kJ/mol and the rate constant for the peak temperature was found to be comparable to that of $Ge_2Sb_2Te_5$ [12]. The crystallization process appears to proceed via a bulk multi-step crystallization mechanism, where the nucleation rate increases with time [13].

To further understand the KSb_5S_8 system, we investigated the isostructural solid solutions of the type $K_{1-x}Rb_xSb_5S_8$. By partially substituting K for Rb, the properties can be subtly altered while preserving the structure and the phase-change capacity. For example, the same structure forms with K^+, Rb^+, and Tl^+ and thus it is possible to prepare solid solutions of the type $K_{1-x}Rb_xSb_5S_8$ and $K_{1-x}Tl_xSb_5S_8$ [11]. These represent small but significant perturbations on the parent phase that could allow a better assessment of how changes in ionic bonding affect the phase change and other properties of KSb_5S_8. Such studies could lead to a deeper understanding of the relationship of ionic vs. covalent bonding and crystallization kinetics in phase-change materials.

Here, we report on the evolution of physical, thermal, and phase-change properties of a representative set of $K_{1-x}Rb_xSb_5S_8$ solid solutions. The Tl analog showed marked differences in chemical phase change behavior vis-à-vis KSb_5S_8. Using bulk samples we also performed Raman and optical spectroscopic studies recorded during a phase-change event. We discuss structure–property relationships through local structure studies using pair distribution function analysis (PDF), electronic structure, and bonding analysis using density functional theory (DFT) band structure calculations. In addition, we report thermal conductivity measurements for both forms of KSb_5S_8. Generally, the thermal conductivity of phase-change switching materials needs to be low to avoid cross talk during read/write events and in the case of $K_{1-x}Rb_xSb_5S_8$ we show that it is one of the lowest values known for dense solid-state materials.

2. Experimental section

2.1. Reagents

K_2S and Rb_2S were prepared by the reaction of a stoichiometric mixture of potassium or rubidium metal and sulfur in liquid ammonia at -78 °C until no trace of the metal was left (approx. 12 h). The ammonia was then allowed to evaporate and the resulting pale yellow powder was dried under vacuum for 24 h.

Sb_2S_3 was prepared by reacting a stoichiometric mixture of Sb and S powders in an evacuated silica tube at 750 °C for 24 h, then quenched in air to room temperature.

$K_{1-x}Rb_xSb_5S_8$ solid solutions were prepared by a stoichiometric combination of potassium sulfide, rubidium sulfide, and antimony sulfide, where the potassium sulfide to rubidium sulfide ratio was allowed to vary. A mixture of K_2S (1−x mmol, 0 < x < 1), Rb_2S (x mmol), and 1.698 g Sb_2S_3 (5.00 mmol) was loaded in a silica tube under a dry

a

b

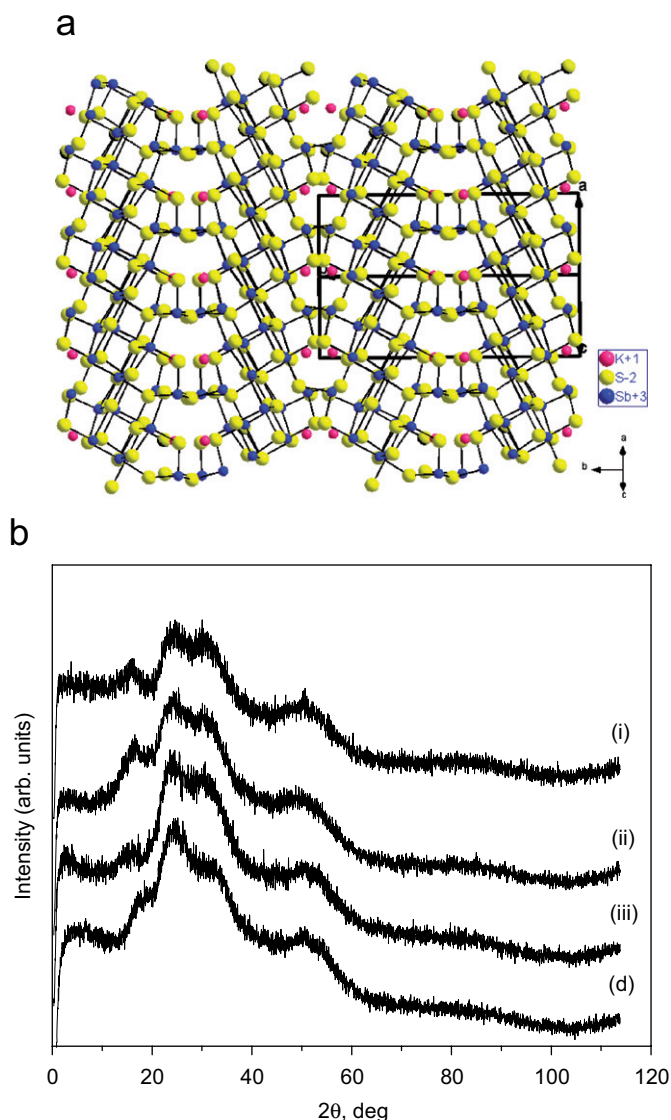Fig. 1. (a) Structure of KSb_5S_8 viewed down the [101] direction. (b) Powder X-ray diffraction patterns of as-synthesized glasses of $K_xRb_{1-x}Sb_5S_8$ (i–iii, x = 0.25, 0.5, 0.75, respectively) and $TlSb_5S_8$ (iv), showing their amorphous nature.

nitrogen atmosphere in a Vacuum Atmospheres Dri-Lab glovebox and flame-sealed under reduced pressure ($<10^{-4}$ mbar). The mixture was heated in a flame until a homogeneous, orange melt was achieved, which was then quenched in air to form a silver, glassy ingot. The yield was quantitative. Crystalline $K_{1-x}Rb_xSb_5S_8$ was formed by annealing the glassy ingot above the crystallization point, which ranged from 278 to 314 °C depending on composition.

Glassy $TlSb_5S_8$ was prepared by the reaction of a stoichiometric combination of Tl metal, Sb_2S_3, and sulfur powder. The reactants were loaded into in a silica tube under a dry nitrogen atmosphere in a Vacuum Atmospheres Dri-Lab glovebox and flame-sealed under reduced pressure ($<10^{-4}$ mbar). The mixture was heated in a furnace at 800 °C for 1 d, then quickly removed and quenched in ice water to afford the $TlSb_5S_8$ glass.

2.2. Electron microscopy

Quantitative microprobe analyses of the compounds were performed with a JEOL JSM-35C scanning electron microscope (SEM) equipped with a Tracor Northern energy-dispersive spectroscopy (EDS) detector. Data were acquired using an accelerating voltage of 25 kV and a 1-min acquisition time.

2.3. Powder X-ray diffraction

The samples were examined by X-ray powder diffraction for identification and to assess phase purity. Powder patterns were obtained using a CPS 120 INEL X-ray powder diffractometer with Ni-filtered Cu Kα radiation operating at 40 kV and 20 mA and equipped with a position-sensitive detector. The purity of phases was confirmed by comparison of the X-ray powder diffraction patterns to ones calculated from single crystal data using the NIST Visualize 1.0.1.2 software.

2.4. Synchrotron radiation diffraction experiments

Synchrotron radiation scattering experiments were carried out at the beamline 11-ID-C at the Advanced Photon Source at Argonne National Laboratory using X-rays of energy 115.68 keV ($\lambda = 0.1072$ Å). The higher energy X-rays were used to obtain diffraction data to higher values of the wave vector, Q, which is important for the success of atomic PDF analysis. The measurements were carried out in symmetric transmission geometry and scattered radiation was collected with an intrinsic germanium detector connected to a multi-channel analyzer.

2.5. Thermal analysis

Differential thermal analysis (DTA) was performed with a computer-controlled Shimadzu DTA-50 thermal analyzer. The crushed powders (~25 mg total mass) were sealed in silica ampoules under reduced pressure ($<10^{-4}$ mbar). A silica ampoule of equal mass was sealed and placed on the reference side of the detector. The samples were heated to 850 °C at a rate of 10 °C/min where they were isothermed for 5 min followed by cooling at 10 °C/min to room temperature.

The differential scanning calorimetric (DSC) measurements were carried out with a Setaram DSC141 calorimeter. Temperature and energy calibrations of the instrument were performed, for different heating rates, using the well-known melting temperatures and melting enthalpies of high-purity zinc and indium supplied with the instrument. Bulk-shaped specimens weighing about 7 mg were crimped in aluminum crucibles; an empty aluminum crucible was used as reference. A constant flow of nitrogen was maintained to provide a constant thermal blanket within the DSC cell, thus eliminating thermal gradients and ensuring the validity of the applied calibration standard from sample to sample. In the DSC measurements, the heating rate was 10 °C/min.

2.6. Raman scattering

Raman spectra were measured on a Jobin-Yvon LABRAM 28 spectrometer equipped with a LINKAM high-temperature cell. To eliminate artifacts from oxidative sample decomposition, all the experiments were repeated with the samples sealed in silica ampoules. A solid-state diode laser was used for all measurements, generating 10 mW power at an excitation wavelength of 785 nm. Scattered radiation was collected with a CCD. For each run, two scans were accumulated at a scanning time of 60 s, generating a spectrum with a resolution of $0.7 \, cm^{-1}$. Raman spectra were also obtained with a Holoprobe Raman spectrograph equipped with a CCD camera detector using 633 nm radiation from a HeNe laser for excitation and a resolution of $1 \, cm^{-1}$.

2.7. Thermal conductivity measurements

The thermal conductivity was determined with a longitudinal steady-state method over the temperature range 4–300 K. In this case, samples were attached (using either a low melting point solder or silver-loaded epoxy) to the cold tip of the cryostat, while the other end of the sample was provided with a small strain gauge resistor (thin film), which serves as a heater. Temperature difference across the sample was measured using differential chromel-constantan thermocouple. Both crystalline and glassy KSb_5S_8 materials were measured. The polycrystalline samples were cylindrical in shape with diameter 4 mm and length about 5 mm. Radiation loss is an unavoidable error in all thermal conductivity measurements made using a longitudinal steady-state technique manifested in deviations from the true value that increase with temperature above about 200 K. In order to determine the radiation loss experimentally, we made a subsequent measurement with the sample

detached from the heat sink (sample hangs by thin connecting wires). We determined the amount of heat needed to supply to the heater that raises the temperature of the entire sample to the same average temperature as during the actual measurement of the thermal conductivity. The values of the thermal conductivity were then corrected for this radiation loss.

2.8. Electronic structure calculations

Electronic structure calculations were performed using the self-consistent full-potential linearized augmented plane wave (LAPW) method [14] within DFT [15], using the generalized gradient approximation (GGA) of Perdew et al. [16] for the exchange and correlation potential. Convergence of the self-consistent iterations was performed for 20 k points inside the irreducible Brillouin zone to within 0.0001 Ry with a cutoff of -6.0 Ry between the valence and the core states. Scalar relativistic corrections were included and a spin–orbit interaction was incorporated using a second variational procedure [17]. The calculations were performed using WIEN2K program [18].

3. Results and discussion

3.1. Phase-change behavior

Solid solutions of the form $K_{1-x}Rb_xSb_5S_8$ were synthesized with $x = 0$, 0.25, 0.5 and 0.75 by quenching the corresponding melts in air or water. They were obtained as shiny, gray metallic-like glasses, which are red-purple in fine powdered form and are amorphous by powder X-ray diffraction (Fig. 1(b)). The crystalline phases exhibit the same color difference between bulk and powder, though the crystalline form is a dull, silvery ingot rather than mirror-like. Powder X-ray diffraction of these samples obtained after annealing above the crystallization temperature showed them to be isostructural to the parent KSb_5S_8 [19]. The increasing incorporation of the larger Rb atom in $K_{1-x}Rb_xSb_5S_8$ is confirmed by the shift of the (200) reflection in the X-ray diffraction pattern from $9.03°$ to $8.60°$ in 2θ (Fig. 2).

The effect of this substitution on the thermal properties of the materials was measured with DTA and DSC experiments. We observe systematic evolution of the crystallization as a function of temperature, and in some cases incongruent melting as indicated by the two melting endotherms. The thermograms of the four different samples with $x = 0$, 0.25, 0.50 and 0.75 are presented in Fig. 3 where the glass transition (T_g), the crystallization peak (T_p) and the melting point (T_m), considered as the onset of melting peak, temperatures are shown. There is a pronounced differentiation in phase-change behavior as the Rb fraction increases in the compound. As shown by the sharp exothermic crystallization peaks in the range 280–310 °C, each of these glasses is a phase-change material with a well-defined crystallization process.
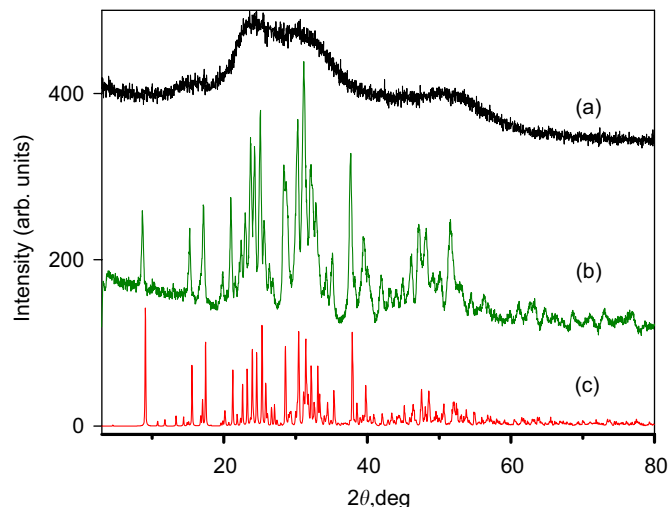

Fig. 2. X-ray diffraction patterns of: (a) $K_{0.25}Rb_{0.75}Sb_5S_8$ glass, as-synthesized. (b) $K_{0.25}Rb_{0.75}Sb_5S_8$ after annealing for 2 h at 300 °C. (c) KSb_5S_8 calculated from crystal structure (monoclinic Pn; $a = 8.1374$ Å; $b = 19.5013$ Å; $c = 9.0620$ Å) [11]. The difference in low-angle peak ((020) reflection) between the pure K structure and the 75% Rb structure is $0.402°$ in 2θ.

The melting point decreases with Rb enrichment (Fig. 4), which is most probably due to the larger size of Rb^+ as compared to K^+ (1.60 Å vs. 1.51 Å) giving rise to longer and weaker $Rb \cdots S$ bonds thereby softening the lattice. This follows the general trend in alkali metal chalcogenides of a decrease in melting point with increasing alkali metal size [20]. This trend is followed until $x = 0.50$ (eutectic point) and then it reverses as we move towards pure $RbSb_5S_8$. A similar trend is observed in the crystallization peaks. The increase of x (Rb content) up to 0.25 results in quite a small shift of the crystallization peak to lower temperatures, and then for $x > 0.25$ is observed a shift to higher temperatures, indicating a minimum value at about $x = 0.25$. The shifts in crystallization temperature could be attributed to a destabilization of the glass up to a minimum between $x = 0.25$ and 0.50 (melting point temperature trend), and then a "locking in" of the structure nearing total K occupancy leading to the increase in the crystallization temperature.

The compounds $TlSb_5S_8$ and $RbSb_5S_8$ were not examined in-depth because of their propensity to phase separate when undergoing transitions, both in melting and crystallization. The glass formed by melting a stoichiometric mixture of Rb_2S and Sb_2S_3 and quenching it in water was found to recrystallize incongruently at 311 and 391 °C, respectively, before melting at 421 °C (Fig. 5(a)). Annealing the Rb-containing glass at 320 °C showed crystallization to $RbSb_5S_8$, $RbSbS_2$, and Sb_2S_3, as determined with X-ray diffraction.

The initial glass of $TlSb_5S_8$ crystallizes at 294 °C and melts rather congruently at 417 °C (Fig. 5(b) and 5(c)). Upon cooling, however, a mixture of the crystalline phases $TlSbS_2$, Sb_2S_3, and $TlSb_5S_8$ were identified. This is

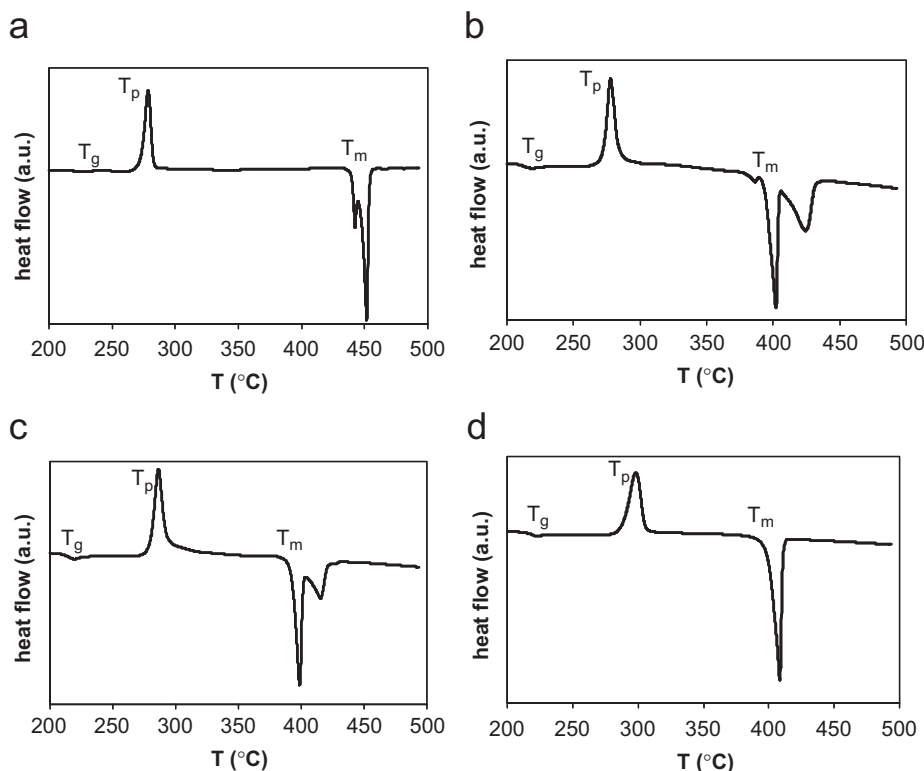Fig. 3. (a) DSC thermograms of $K_{1-x}Rb_xSb_5S_8$ amorphous alloys with heating rate 10 °C/min. (a) $x = 0.0$, (b) $x = 0.25$, (c) $x = 0.5$, and (d) $x = 0.75$. The glass transition (T_g) was determined by the intersection of the curve and the half-way line between the two base lines.
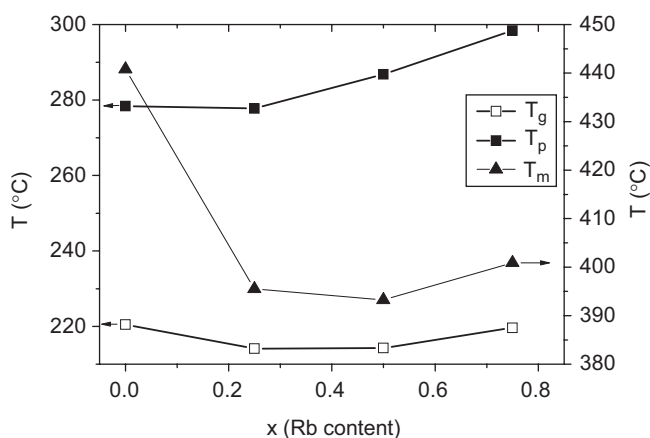

Fig. 4. Dependence of the glass transition (T_g), crystallization peak (T_p) and the onset of melting point (T_m) on the Rb content (x).

consistent with the phase diagram of the Tl_2S/Sb_2S_3 reported previously [21].

3.2. Glass-forming ability (GFA)

GFA as related to the ease of devitrification is a crucial property for understanding the origins of glass formation and also important for designing and developing new bulk glasses [22]. In $K_{1-x}Rb_xSb_5S_8$, following the initial heating treatment, the samples were cooled from 500 °C to RT at rates 10 and 25 °C/min. It was observed that the parent

KSb_5S_8 phase ($x = 0$) crystallizes completely upon slow cooling (10 or 25 °C/min) from 500 °C, whereas for $x = 0.25$ and 0.50 the compound crystallizes partially under these conditions and complete vitrification was observed for $x = 0.75$. Thus, the incorporation of Rb tends to enhance GFA.

The GFA of a melt is evaluated in terms of critical cooling rate (R_c) for glass formation, which is the minimum cooling rate necessary to keep the melt amorphous without precipitation of crystals during solidification. The smaller the R_c, the higher the GFA of a system; however, R_c is a parameter that is difficult to measure precisely. As a result, many criteria have been proposed to reflect the relative GFA on the basis of the characteristic temperatures measured by DTA [23]. The most extensively used criteria are the reduced glass transition temperature T_{rg} (glass transition temperature T_g over liquidus temperature T_l or melting temperature T_m) and the supercooled liquid region ΔT_{xg} (the temperature difference between the onset crystallization temperature T_x and the glass transition temperature T_g). Generally, the larger the temperature interval ΔT_{xg} the higher the GFA. Another parameter K_{gl} suggested by Hruby [24] is also used as a measure of the glass-forming tendency of materials:

$$K_{gl} = (T_x - T_g)/(T_m - T_x) \qquad (1)$$

or K'_{gl} where T_l instead of T_m is used [25]. According to Hruby, the higher the value of K_{gl} in a glass, the higher is
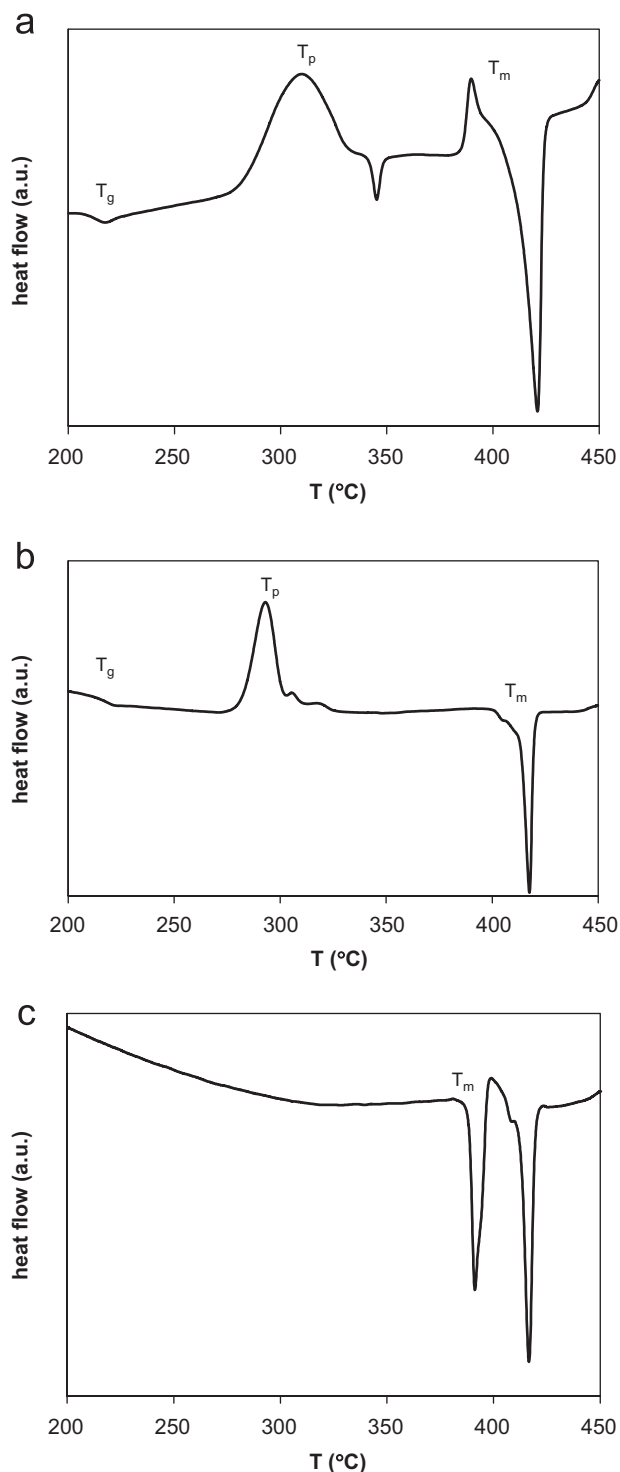
a

b

c

Fig. 5. DSC thermograms with heating rate 10 °C/min: (a) $RbSb_5S_8$, (b) $TlSb_5S_8$ first heating, and (c) $TlSb_5S_8$ second heating.

Table 1
Dependence on the reduced glass transition temperature T_{rg}, the supercooled liquid region ΔT_{xg} and Hruby parameters K_{gl} and K'_{gl} from Rb content for $K_{1-x}Rb_xSb_5S_8$[a]

$K_{1-x}Rb_xSb_5S_8$ $x(Rb)$	T_{rg}	ΔT_{xg} (K)	K_{gl}	K'_{gl}
0.00	0.68	52.7	0.31	0.29
0.25	0.69	58.5	0.48	0.37
0.50	0.71	65.9	0.58	0.48
0.75	0.72	69.9	0.61	0.56

[a]At a heating rate of 10 °C/min.

stabilization means that the melt need not be cooled as quickly to afford the glass and implies a much higher energy barrier of atomic realignment towards the crystal resulting in a slower crystallization speed. This effect is believed to be caused by the greater polarizability and larger size of the Rb atom as compared to K, which results in lower mobility in the lattice and slows down the conversion process to the ordered crystalline phase. Furthermore, the longer Rb···S bonds and increased structural disorder of the solid solution result in a decreased absolute lattice energy compared to the pristine KSb_5S_8. This diminishes the thermodynamic driving force to transform from the higher energy glass state to the lower lying crystalline state.

3.3. Local structure: crystal versus glass

The structures of crystalline and glassy KSb_5S_8 and several $K_{1-x}Rb_xSb_5S_8$ compositions were probed with X-ray scattering using PDF analysis [26]. Deeper structural clues were sought as to the nature of glass vis-à-vis crystal by investigating similarities and differences in the structure of both forms at the atomic level. The atomic PDF technique has emerged recently as a powerful tool for the characterization and structure refinement of materials with intrinsic disorder. The utility of the technique stems from the fact that it takes into account *the total diffraction*, that is Bragg as well as diffuse scattering, and so it can be applied to both crystalline [27] and amorphous materials [28]. Therefore, the technique is both a local and an extended structure probe and thus a powerful tool that can be used to identify differences in structural features between the crystalline and glassy versions of these materials [29].

The PDF, $G(r)$, is obtained from the experimentally determined total-scattering structure function, $S(Q)$, by a sine Fourier transform

$$G(r) = \frac{2}{\pi} \int_0^\infty Q[S(Q) - 1]\sin(Qr)\,\mathrm{d}Q$$
$$= 4\pi r[\rho(r) - \rho_0],$$

where r is the distance between two atoms and Q the magnitude of the scattering vector, and $S(Q)$ is the corrected and properly normalized powder diffraction

its stability against crystallization on heating and, presumably the higher its vitrifiability on cooling.

In Table 1, we present the values of all the characteristic parameters (T_{rg}, ΔT_{xg}, K_{gl}, K'_{gl}) for the $K_{1-x}Rb_xSb_5S_8$ system. All the calculated parameters increase with the decrease in the K^+ ion fraction, indicating that glass stability and GFA increase with an increase in x. This

pattern of the material (also called the structure function). $\rho(r)$ and ρ_0 are the local and average atomic number densities, respectively, and r is the radial distance. Experimental structure functions $S(Q)$ for crystalline and glassy KSb_5S_8 are shown in Fig. 6 on an absolute scale. The structure of crystalline KSb_5S_8 was analyzed and refined based on the PDF data to obtain a basis for the structural comparisons of the glass forms and the results were in excellent agreement with those of the single crystal refinement [11]. In the glass, the Bragg peaks are lacking and only diffuse scattering is observed; however, the

scattering profile tracks closely the profile of the crystalline form. Beyond $8\,\text{Å}^{-1}$, both scattering patterns merge into a slowly oscillating diffuse component.

The experimental PDFs for both forms of KSb_5S_8 are shown in Fig. 7(a) and (b), respectively. They were obtained from the synchrotron radiation diffraction data following the usual data reduction procedures described previously [27]. As can be seen in Fig. 7 the experimental PDFs peak at characteristic distances separating pairs of atoms and thus reflect the local atomic-scale structure. In the crystalline phase, these molecular units are arranged into a 3D periodic structure and the corresponding experimental PDF oscillates out to high interatomic vectors (see Fig. 7(a)). In particular, the first peak in both PDFs is located between 2.4 and 2.8 Å reflecting the Sb–S bonds in the sample. As determined from the crystal structure of KSb_5S_8, there are several SbS_6 and SbS_7 coordination polyhedra with a spread of Sb–S bond lengths. One typical such fragment is shown in Fig. 7(d). The second and third PDF peaks occur at approximately 4 and 6 Å and reflect mostly the nearest Sb–Sb and S–S atomic neighbor distances and possibly some longer Sb–S distances. The three PDF peaks, which occur within the first 7 Å, correspond to a well-defined and compact structural fragment of "SbS_7" shown in Fig. 7(d). The calculated PDF of the molecular "SbS_7" fragment is shown for comparison in Fig. 7(c). It is clear that the three correlation peaks due to Sb–S bond and S–S second neighbor distances are very similar to those observed experimentally (Fig. 7(a) and (b)). The PDFs of the
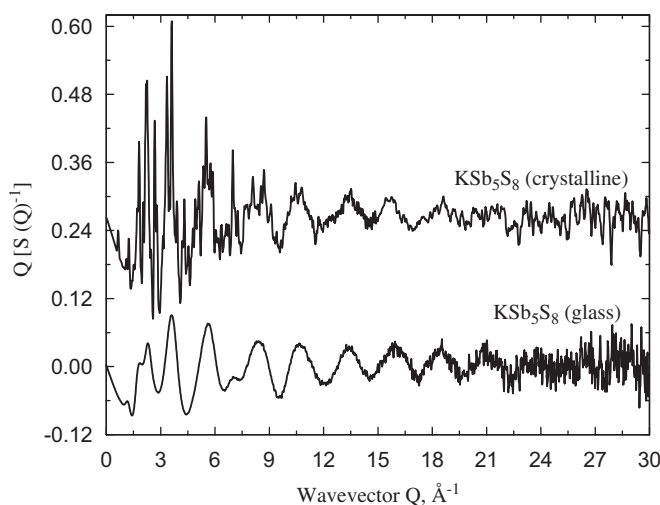

Fig. 6. Experimental structure functions of crystalline and glassy KSb_5S_8.

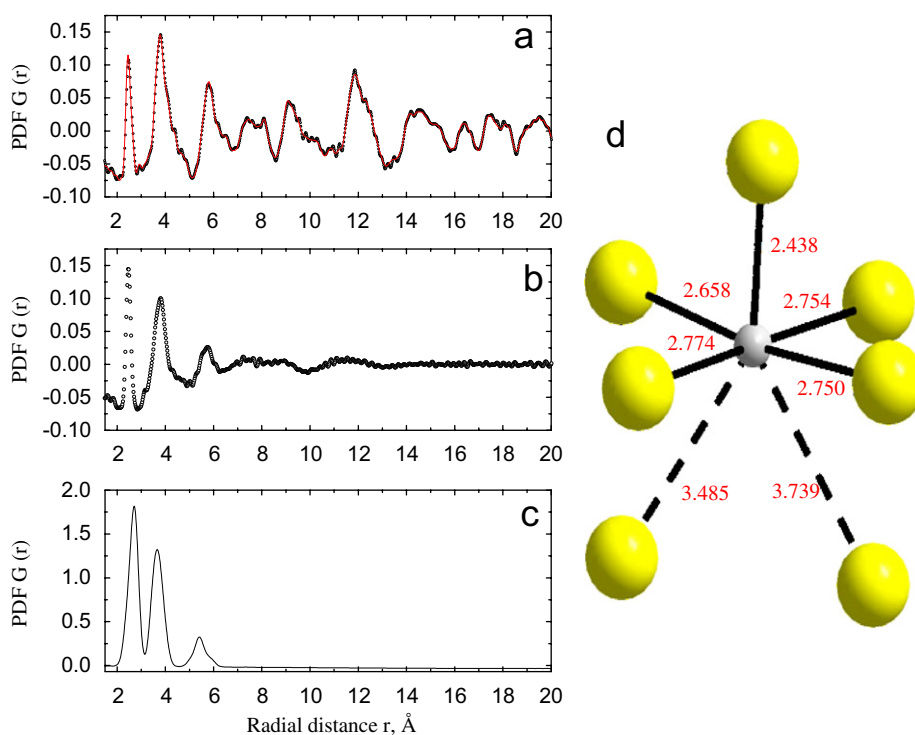Fig. 7. (a) PDF plot of crystalline KSb_5S_8, experimental: black dots, calculated: red line, (b) PDF plot of glassy KSb_5S_8, (c) Sb coordination environment in KSb_5S_8.

$K_{1-x}Rb_xSb_5S_8$ members (not shown) were similar to that of the parent compound suggesting they possess the same local structure.

In the glass, the experimental PDF is seen to decay to zero at ~15 Å. Obviously, its structural coherence length is much shorter than that observed in the crystal. This coherence length, however, is much longer than those of more conventional glasses such as SiO_2 and underscores a much more organized and well-defined local structure in the amorphous $[Sb_5S_8]^-$ framework. Based on the strong similarity of the $G(r)$ of the two forms up to 7 Å, see Fig. 7(a) and (b), we surmise that this structural fragment is essentially invariant in both the glass and the crystal. The glass structure consists essentially of the same rigid SbS_n fragments as the crystalline KSb_5S_8 structure except that they are connected in a disordered fashion. If the basic building units that define the structure of KSb_5S_8 are intact in the glass, only a small reorganization would be required to regain the periodic crystalline state. This is consistent with the rapid and facile crystallization processes in this system.

3.4. Electronic absorption and Raman spectroscopy

The effect of the substitution of Rb^+ into the structure on the electronic properties was probed with optical reflectance spectroscopy in the glasses (Fig. 8). Each glass member showed a band gap $E_g \sim 1.50$ eV, which is slightly lower than that of the parent KSb_5S_8 glass of 1.67 eV. There was no significant variation in the experimentally measured band gaps of the solid solutions as a function of x which may be due to the competing effects of the larger, more polarizable nature of the Rb^+ ion, which should decrease the band gap, and the increased ionicity of the more electropositive Rb^+ ion, which should increase it. This is consistent with the bonding insights obtained by the
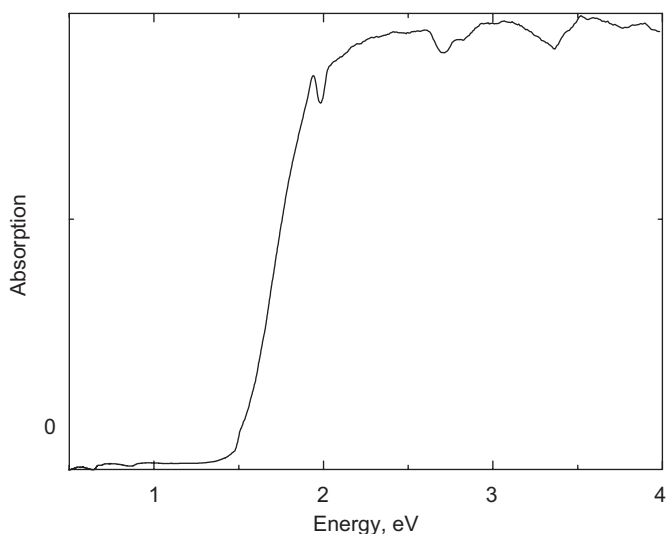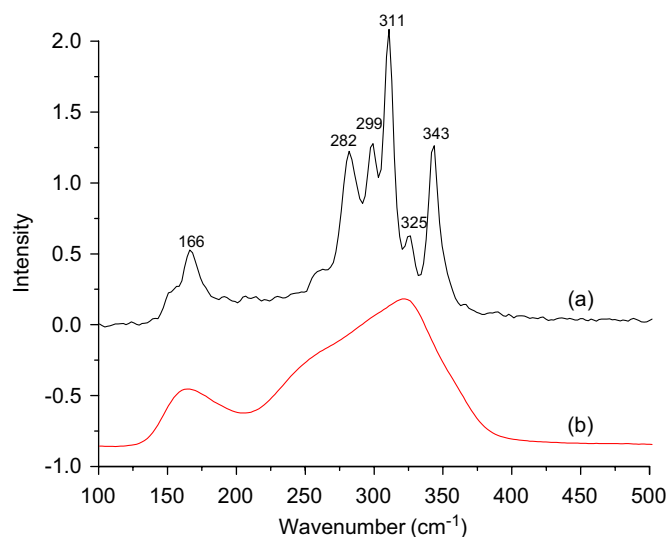

Fig. 9. Raman scattering data on crystalline and glassy KSb_5S_8 at room temperature.
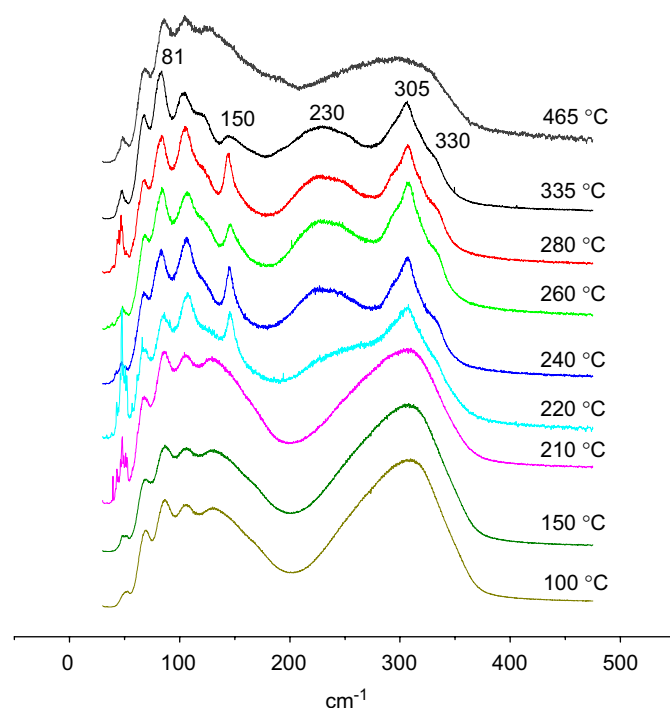

Fig. 10. Raman scattering data of glassy KSb_5S_8 at various temperatures along the heating curve. The crystallization event is shown by the rapid sharpening of peaks between 240 and 310 °C.

electronic band structure calculations on KSb_5S_8 presented below.

Fig. 9 compares the Raman spectra of glassy and crystalline KSb_5S_8 measured at room temperature. While the crystalline material shows five well-defined peaks between 280 and 345 cm^{-1}, which can be attributed to vibrations involving the $[Sb_5S_8]^{1-}$ framework, the spectrum observed in the glass is extremely broad, suggesting a wide distribution of bond angles. Nevertheless, the centers of

Fig. 8. Solid state UV–vis reflectance spectrum of $K_{0.75}Rb_{0.25}Sb_5S_8$ converted to absorption via the Kubelka–Munk procedure. The spectra for $K_{0.5}Rb_{0.5}Sb_5S_8$, and $K_{0.25}Rb_{0.75}Sb_5S_8$ glasses are similar. The energy gaps are 1.50, 1.47, and 1.51 eV, respectively.

gravity of both spectra roughly coincide, supporting the close structural resemblance of both phases inferred from the PDF study discussed above. The amorphous KSb_5S_8 phase at room temperature shows Raman shifts on top of a broad feature centered at ~ 100–$150\,cm^{-1}$ and a characteristic broad peak in the 250–$350\,cm^{-1}$ range. Essentially identical room temperature spectra were observed for the mixed-alkali $K_{1-x}Rb_xSb_5S_8$ glasses, further supporting the interpretation that all of these spectral features can be attributed to vibrations involving only the framework atoms of antimony and sulfur.

To obtain further insight into the local structure of the glass and the phase-change process, we conducted temperature-dependent Raman scattering experiments in an attempt to observe the crystallization process in situ. The Raman spectra as a function of temperature of a KSb_5S_8 glass sample are shown in Fig. 10. As long as the temperature remained below the glass transition temperature of $220\,°C$, no significant changes were observed in the Raman spectra of the glass. Above T_g, well-defined features are observable, which are successively developed above $240\,°C$. The new features include intense peaks at 81 and $150\,cm^{-1}$, as well as features near 230 and $305\,cm^{-1}$ with a shoulder near $330\,cm^{-1}$. When the temperature exceeded the compound's melting point, this spectrum disappeared giving rise to a similar one observed for the glass at room temperature.

While the nucleation of crystals above T_p is easily detected in the Raman spectra, the comparison of the spectra above $240\,°C$ (Fig. 10) with that of the fully crystallized material (Fig. 9(a)) reveals that the sharpening of these Raman peaks is only gradual. That the Raman peaks do not entirely sharpen in this temperature region indicates that the nucleated material is still strongly disordered above T_p, and extra energy is needed to fully crystallize and "lock" the atoms into their crystallographic coordinates. DTA studies conducted on KSb_5S_8 during melt cooling reveal no crystallization exotherms, suggesting the formation of glassy material under these conditions [10]. Nevertheless, Raman spectra obtained during melt cooling (Fig. 11) reveal the same features as those obtained above T_p during the heating cycle, indicating that small crystalline nuclei have formed under these (relatively slow) cooling conditions. This is most clearly seen by the appearance of peaks near 338, 321, 310, 298, and $280\,cm^{-1}$ (reflecting peak positions observed in crystalline KSb_5S_8) which become increasingly well-defined with decreasing temperature. The sizes of the nuclei generally depend on the cooling rate and in the case of the Raman experiments the cooling rate was considerably slower that those used in the DTA experiments ($10°$/min).

3.5. Thermal conductivity

In phase-change materials, besides optical response, the thermal behavior is important for reasons involving heating, quenching and switching speeds, cyclability and suppression of thermal cross talk [30]. A low thermal conductivity is necessary to ensure fast, localized heating over a minimum area. Optimization for thermal performance requires accurate knowledge of the thermal conductivity of both glass and crystalline states and it is therefore imperative to have an accurate estimation of the thermal transport properties of these materials. The thermal conductivity of bulk crystalline and glassy KSb_5S_8 was measured with a steady-state technique over the
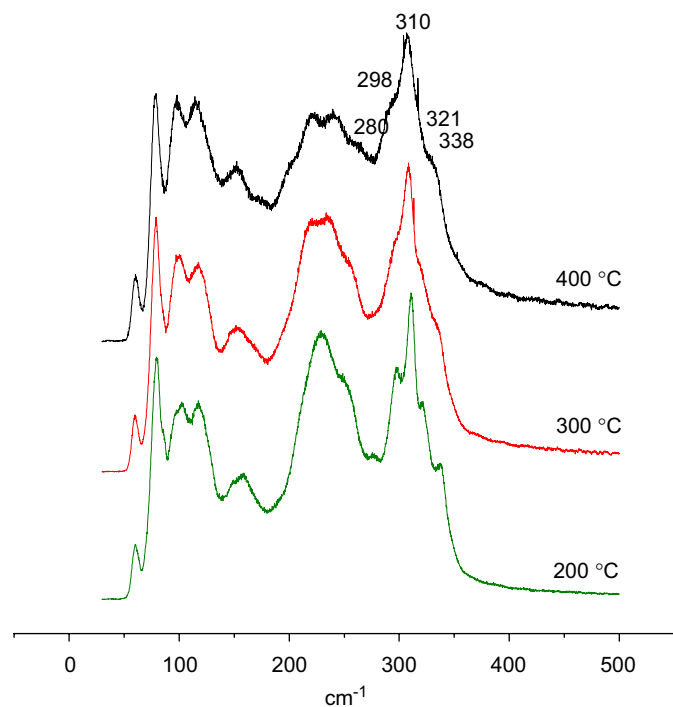

Fig. 11. Raman scattering data of KSb_5S_8 cooled from the molten state. Crystallization is evidenced by the sharpened features near 338, 321, 310, 298, and $280\,cm^{-1}$.
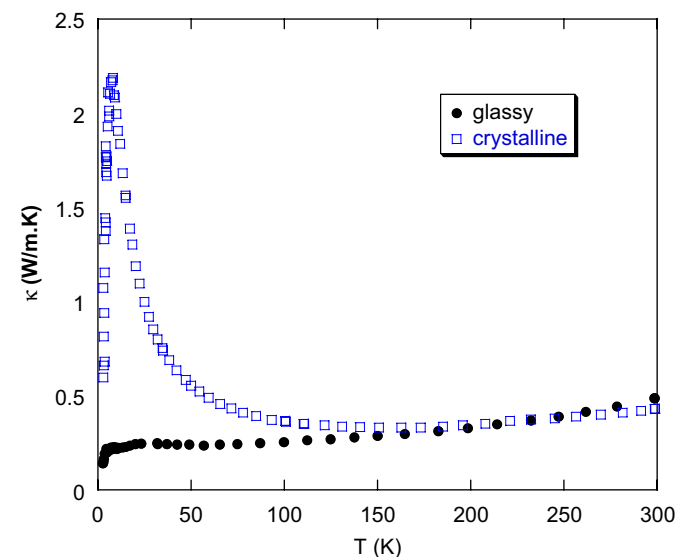

Fig. 12. Temperature dependence of thermal conductivity of the crystalline and glassy KSb_5S_8 (4–300 K).

temperature range of 4–300 K (Fig. 12). Because both forms of KSb_5S_8 have a very low electrical conductivity (e.g. $< 10^{-8}$ S/cm) the data shown essentially represent the lattice thermal conductivity.

The thermal conductivity of crystalline KSb_5S_8 exhibits the expected Umklapp peak at low temperatures (about 8 K) and is characteristic of crystalline materials [31]. It is caused by the competition between the phonon-boundary scattering and Umklapp phonon–phonon interactions. On the other hand, glassy KSb_5S_8 shows no such peak at low temperatures, which is a typical behavior for amorphous materials and presents significantly lower values as expected due to the structural disorder [32].

At higher temperatures, the thermal conductivity for both samples is similar regarding both magnitude and trend. The thermal conductivity of crystalline KSb_5S_8 at room temperature is an amazingly low 0.4 W/m K. This value in fact represents an upper bound in this family of materials as we expect the solid solutions $K_{1-x}Rb_xSb_5S_8$ to be even less thermally conducting.

The thermal conductivity of KSb_5S_8 is lower than that of $Ge_2Sb_2Te_5$, which is 0.55 W/m K [33]. This may appear surprising since KSb_5S_8 consists of lighter elements than $Ge_2Sb_2Te_5$ and is generally expected to have higher lattice thermal conductivity [34]. The lower values in the sulfide compound can be attributed to the characteristically lower crystal symmetry, the relatively large unit cell, and the presence of weakly bound K atoms (i.e. $K \cdots S$ ionic bonding). All these are absent in $Ge_2Sb_2Te_5$. This finding implies that in certain cases KSb_5S_8 may have an advantage over $Ge_2Sb_2Te_5$ in sustaining smaller spot sizes, and higher packing densities without thermal cross talk.

4. Electronic structure calculations

Electronic structure calculations were performed for KSb_5S_8 and $TlSb_5S_8$ in order to investigate the effect of the K and Tl atoms on the electronic properties of the $[Sb_5S_8]^-$ framework. The band structure results show that both systems are indirect band gap semiconductors with similar band gap sizes and assess the extent of ionic bonding. The gap in KSb_5S_8 is 1.55 eV, whereas $TlSb_5S_8$ has a slightly lower value of 1.50 eV, see Fig. 13. This suggests that the covalent interaction of Tl atoms with the $[Sb_5S_8]^-$ framework is slightly stronger than that of K atoms.

Density of states (DOS) analysis shows that the valence bands for both the systems consist mostly of sulfur p orbitals, which hybridize with the Sb *p* and *s* orbitals (Fig. 14(c)–(f)). In KSb_5S_8, the conduction band states lying below 5 eV consist mostly of hybridized Sb *p* and S *p* orbitals and the K *s* orbitals are located well above 5 eV (Fig. 14(c) and (e)), consistent with primarily ionic $K \cdots S$ interactions. On the other hand, the conduction band below 5 eV of $TlSb_5S_8$ consists of Sb *p*, S *p*, and Tl *p* hybridized orbitals. This shows that the covalent interaction between Tl and Sb–S framework is more significant than the $K \cdots S$ interaction (Fig. 14(d) and (f)) [35].

In order to quantitatively describe the covalent interactions between the K and Tl atoms with the Sb–S framework, we performed crystal orbital Hamilton population (COHP) analysis, which is a bond-detecting tool for solids and molecules. COHP partitions the band structure energy (in terms of the orbital pair contributions) into bonding, non-bonding, and antibonding energy regions within a specified energy range [36]. Positive values of –COHP describe bonding energy regions whereas negative values describe antibonding energy regions. The integrated values of –COHP (–ICOHP) up to the Fermi energy give the energy contribution of the bonds to the total energy. Large positive values for –ICOHP correspond to strong covalent bonding interaction.

We have considered the bonding interactions of K and Tl atoms with the nearest S atoms up to a distance of 3.4 Å. For the S6 and S13 atoms, which are two of the nearest to K and Tl atoms, we have also considered the bonding interactions up to 3.4 Å. The value of the –ICOHP for the

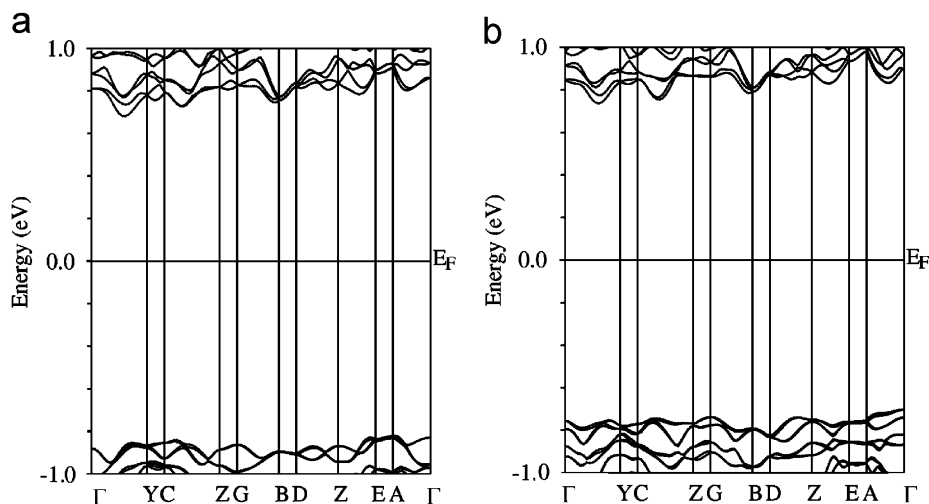Fig. 13. Electronic band structure of (a) KSb_5S_8, and (b) $TlSb_5S_8$.
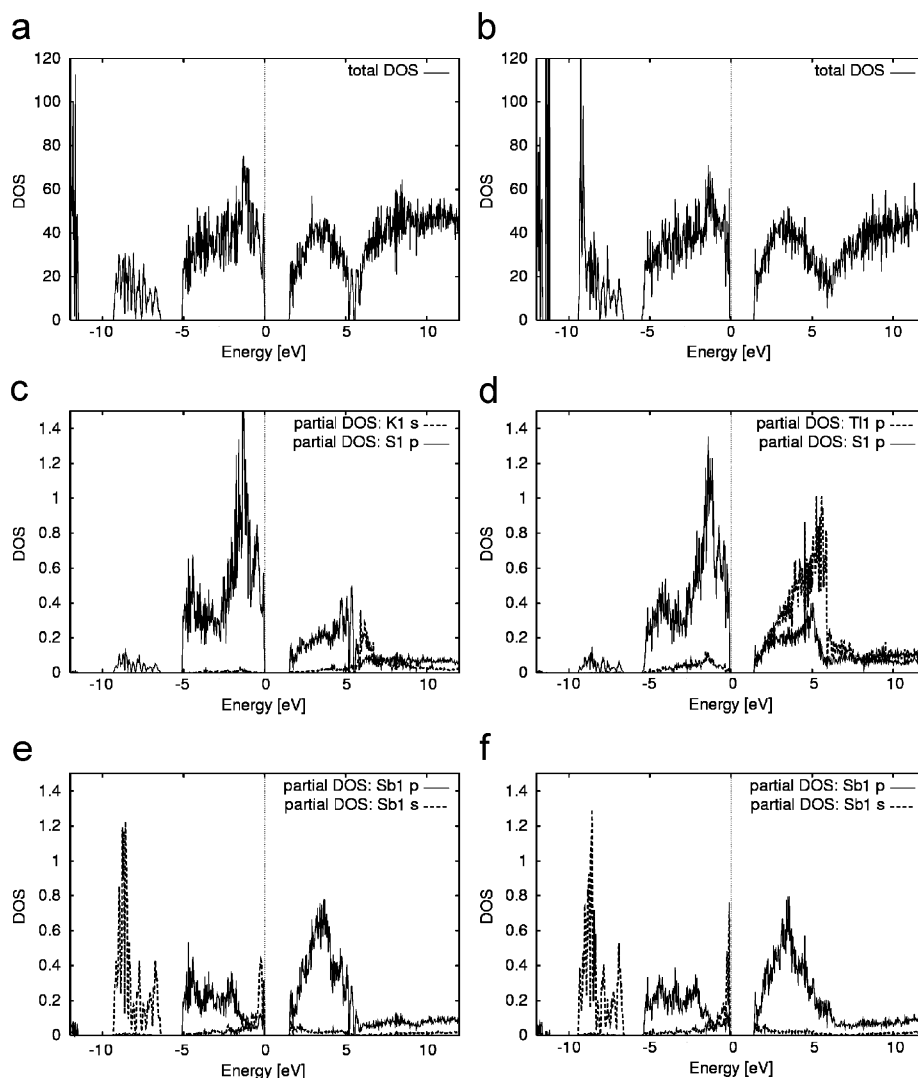
Fig. 14. Total and partial atomic density of states DOS for KSb_5S_8: (a), (c), (e), and for $TlSb_5S_8$: (b), (d), (f).

K interaction with the nearest nine S atoms is 0.56 eV, whereas the corresponding value for Tl is 1.57 eV. This clearly shows a much stronger covalent interaction between Tl and S atoms. The -ICOHP value of the S6 interaction with its nearest four neighbors (Sb2, Sb3, 2 K) for KSb_5S_8 system is 5.07 eV, whereas the value of S6 interaction with its nearest four neighbors (Sb2, Sb3, 2Tl) for $TlSb_5S_8$ is 5.2 eV. The –ICOHP values of the S13 interaction with its nearest five neighbors are 2.11 and 4.96 eV for the KSb_5S_8 and $TlSb_5S_8$, respectively. This is also an indication of a stronger covalent interaction of Tl atoms with the Sb–S framework than that of K atoms.

5. Concluding remarks

The KSb_5S_8 is a good example of a phase-change material with a mixed ionic/covalent bonding. The K site in the structure can be used to modulate the glass-forming properties and crystallization rates of the system via isomorphic substitution with Rb. In this work we introduced perturbations on the ionic bonding i.e. $K(Rb)\cdots S$ part which affects the phase change properties of the system significantly. The members of the $K_{1-x}Rb_xSb_5S_8$ series exhibit phase-change properties with greater GFA than KSb_5S_8. The GFA increases with increasing Rb content. In this case, the random alloy disorder in the alkali metal sublattice seems to predominate over the increased degree of ionicity in going from $K\cdots S$ to $Rb\cdots S$ bonding and works to stabilize the glass forms in $K_{1-x}Rb_xSb_5S_8$ and slow the crystallization process compared to pure KSb_5S_8. Tl ions also substitute for K but the Tl analog itself is not stable on melting and therefore its phase change behavior is relatively complicated. Property modification could not be accomplished with neither Sb nor S site substitution in the structure of KSb_5S_8 as these sites do not lend themselves for similar substitutions with e.g. Bi, Se, respectively. Band structure calculations on KSb_5S_8 and $TlSb_5S_8$ suggest a wide indirect energy gap with the $Tl\cdots S$ interactions being slightly stronger than those of $K\cdots S$.

In-depth studies are needed in chalcogenide systems in which the ionic/covalent bonding ratio can be varied. In this regard, KSb_5S_8 and related $A/Sb/Q$ (A = alkali metal, Q = S, Se) phases could be excellent study cases. Of particular interest would be to compare the behavior of K/Sb/S systems to that of K/Sb/Se counterparts and such studies are currently under way. The glass possesses relatively long-range order (up to 7 Å) compared to most known glasses. The glassy and the crystalline states share large, well-defined local coordination polyhedral "SbS_7" fragments of an approximate length scale of $\sim$7 Å. This represents a substantial degree of built-in pre-organization in the amorphous form that sets the stage for facile crystallization. Finally, the thermal conductivity of both glass and crystalline KSb_5S_8 is among the lowest known for any dense inorganic solid-state material.

Acknowledgments

References

[1] (a) L. Hesselink, A. Mijiritskii (Eds.), Advanced data storage materials and characterization techniques, MRS Proceedings 2003, 803, references therein;
(b) H.J. Borg, R.J. van Woudenberg, Magn. Magn. Mater. 193 (1999) 519–525;
(c) M. Popescu, F. Sava, A. Anghel, A. Lorinczi, I. Kaban, W.J. Hoyer, Optoelectr. Adv. Mater. 7 (2005) 1743–1748;
(d) S. Gidon, O. Lemonnier, B. Rolland, O. Bichet, C. Dressler, Y. Samson, Appl. Phys. Lett. 85 (2004) 6392–6394.

[2] (a) M.H.R. Lankhorst, B.W.S.M.M. Ketelaars, R.A.M. Wolters, Nat. Mater. 4 (2005) 347;
(b) J. Teteris, M. Reinfelde, J. Optoelectron. Adv. Mater. 5 (2003) 1355–1360;
(c) H. Hisakuni, K. Tanaka, Science 270 (1995) 974–975.

[3] (a) A.H. Edwards, A.C. Pineda, P.A. Schultz, M.G. Martin, A.P. Thompson, H.P. Hjalmarson, J. Phys.-Condens. Mater. 17 (2005) L329;
(b) D.H. Ahn, D.H. Kang, B.K. Cheong, H.S. Kwon, M.H. Kwon, T.Y. Lee, J.H. Jeong, T.S. Lee, I.H. Kim, K.B. Kim, IEEE Electron. Dev. Lett. 26 (2005) 286.

[4] T.J. Ohta, Optoelectron. Adv. Mater. 3 (2001) 609.

[5] B. Spektor, M. Lisiansky, J. Shamir, M. Klebanov, V. Lyubin, Appl. Phys. Lett. 76 (2000) 798.

[6] V.K. Tikhomirov, S.R. Elliott, Phys. Rev. B 49 (1994) 17476.

[7] J. Lucas, Curr. Opin. Solid State Mater. Sci. 4 (1999) 181.

[8] (a) N. Yamada, E. Ohno, K. Nishiuchi, N. Akahira, M.J. Takao, Appl. Phys. 69 (1991) 2849;
(b) N. Yamada, T.J. Matsunaga, Appl. Phys. 88 (2000) 7020.

[9] S. de la Parra, L.C. Torres-Gonzalez, L.M. Torres-Martinez, E.J. Sanchez, Non-Cryst. Solids 329 (2003) 104–107.

[10] T. Kyratsi, K. Chrissafis, J. Wachter, K.M. Paraskevopoulos, M.G. Kanatzidis, Adv. Mater. 15 (2003) 1428.

[11] P. Berlepsch, R. Miletich, Th. Armbruster, Z. Kristallogr. 214 (1999) 57.

[12] J. Park, M. Kim, W. Choi, H. Seo, C. Yeon, Jpn. J. Appl. Phys. 38 (1999) 4775.

[13] K. Chrissafis, T. Kyratsi, K.M. Paraskevopoulos, M.G. Kanatzidis, Chem. Mater. 16 (2004) 1932.

[14] D. Singh, Planewaves, Pseudopotential, and the LAPW method, Kluwer Academic, Boston, MA, 1994.

[15] (a) P. Hohenberg, W. Kohn, Phys. Rev. 136 (1964) B864–B871;
(b) W. Kohn, L. Sham, Phys. Rev. 140 (1965) A1133–A1138.

[16] J.P. Perdew, K. Burke, M. Ernzerhof, Phys. Rev. Lett. 77 (1996) 3865.

[17] D.D. Koelling, B. Harmon, J. Phys. C 10 (1977) 3107.

[18] P. Blaha, K. Schwarz, G. Madsen, D. Kvasnicka, J. Luitz, WIEN2K, An Augmented Plane Wave + Local Orbitals Program for Calculating Crystal Properties, Karlheinz Schwarz, Technical University, Wien, Vienna, 2001.

[19] Attempts to prepare solid solutions of KSb_5S_8 with respective Bi and Se substitutions were not successful.

[20] TB. Massalski (Ed.), ASM International (Corporate Author), H. Okamoto (Ed.), Compare Melting Points of A_2Q Systems (A = alkali metal, Q = S, Se, Te): Binary Alloy Phase Diagrams, 1986.

[21] J.-C. Jumas, J. Olivier-Fourcade, N. Rey, E. Pilippot, Rev. Chim. Miner. 22 (5) (1985) 651–665.

[22] D. Turnbull, Contemp. Phys. 19 (1969) 473.

[23] Y. Li, S.C. Ng, C.K. Ong, H.H. Hng, T.T. Goh, Scripta Mater 36 (1997) 783.

[24] A. Hruby, Czech. J. Phys. 78 (1972) 1187.

[25] Z. Zhang, W.H. Wang, Y. Hirotsu, Mater. Sci. Eng. A 385 (2004) 38.

[26] (a) B.H. Toby, T. Egami, Acta Crystallogr. 48A (1992) 336;
(b) T. Egami, J Phys. Chem. Solids 56 (1995) 1407.

[27] V. Petkov, I.-K. Jeong, J.S. Jung, M.F. Thorpe, S. Kycia, S.J.L. Billinge, Phys. Rev. Lett. 83 (1999) 4089.

[28] Y. Waseda, The Structure of Non-crystalline Materials, McGraw Hill, New York, 1980.

[29] S.J.L. Billinge, M.G. Kanatzidis, Chem. Commun. 7 (2004) 749.

[30] T. Ohta, K. Inoue, M. Uchida, K. Yoshioka, T. Akiyama, S. Furukawa, K. Nagata, S. Nakamura, Jpn. J. Appl. Phys. 28 (Suppl. 28-3) (1989) 123.

[31] R. Berman, Thermal Conduction in Solids, Clarendon, Oxford, 1976.

[32] (a) C. Kittel, Phys. Rev. 75 (1949) 972;
(b) R.C. Zeller, R.O. Pohl, Phys. Rev. B 4 (1971) 2029.

[33] P.P. Konstantinov, L.E. Shelimova, E.S. Avilov, M.A. Kretova, V.S. Zemskov, Inorg. Mater. 37 (2001) 662.

[34] D.P. Spitzer, J. Phys. Chem. Solids 31 (1970) 19.

[35] The covalent interactions between Rb and the $[Sb_5S_8]^{1-}$ framework are expected to be very similar to those of K because the electron ionization energy of K (4.34 eV) and Rb (4.17 eV) are closer together and differ considerably from that of Tl (6.11 eV). For this reason we did not perform band calculations on $RbSb_5S_8$.

[36] R. Dronskowski, P.E. Bloechl, J. Phys. Chem. 97 (1993) 8617.